Original paper

Phantom study for ^{90}Y liver radioembolization dosimetry with a long axial field-of-view PET/CT

Lorenzo Mercolli [a,*], Konstantinos Zeimpekis [a], George A. Prenosil [a], Hasan Sari [b], Hendrik G. Rathke [a], Axel Rominger [a], Kunagyu Shi [a]

[a] *Department of Nuclear Medicine, Inselspital, Bern University Hospital, University of Bern, Freiburgstrasse 18, CH-3010 Bern, Switzerland*
[b] *Advanced Clinical Imaging Technology, Siemens Healthcare AG, Lausanne, Switzerland*

ARTICLE INFO

ABSTRACT

Purpose: The physical properties of yttrium-90 (^{90}Y) allow for imaging with positron emission tomography/computed tomography (PET/CT). The increased sensitivity of long axial field-of-view (LAFOV) PET/CT scanners possibly allows to overcome the small branching ratio for positron production from ^{90}Y decays and to improve for the post-treatment dosimetry of ^{90}Y of selective internal radiation therapy.

Methods: For the challenging case of an image quality body phantom, we compare a full Monte Carlo (MC) dose calculation with the results from the two commercial software packages Simplicit90Y and Hermes. The voxel dosimetry module of Hermes relies on the ^{90}Y images taken with a LAFOV PET/CT, while the MC and Simplicit90Y dose calculations are image independent.

Results: The resulting doses from the MC calculation and Simplicit90Y agree well within the error margins. The image-based dose calculation with Hermes, however, consistently underestimates the dose. This is due to the mismatch of the activity distribution in the PET images and the size of the volume of interest. We found that only for the smallest phantom sphere there is a statistically significant dependence of the Hermes dose on the image reconstruction parameters and scan time.

Conclusion: Our study shows that Simplicit90Y's local deposition model can provide a reliable dose estimate. On the other hand, the image based dose calculation suffers from the suboptimal reconstruction of the ^{90}Y distribution in small structures.

1. Background

Nowadays, yttrium-90 (^{90}Y) selective internal radiation therapy (SIRT) is a well-established and effective treatment modality for hepatocellular carcinoma (HCC) and liver metastases of neuroendocrine tumours as well as colorectal cancer [1,2]. SIRT exploits the fact that the blood supply of hepatic malignancies is different compared to normal liver parenchyma. It is therefore possible to target the tumor cells locally through the injection of ^{90}Y microspheres into the arteries of the liver.

Individual dosimetry and treatment planning play a pivotal role in applying SIRT safely and for achieving the best possible treatment outcome. An individual treatment planing and verification is recommended by the EANM position paper [3]. For the pre-treatment dosimetry of SIRT, different methods are part of the clinical standard procedure [4–7]. However, despite being recommended [4,5], there is not yet a standardized protocol for post-treatment verification in the clinical routine [6,8].

The known challenges of imaging ^{90}Y Bremsstrahlung [4,6,9] with single photon emission computed tomography (SPECT) made the use of positron emission tomography (PET) systems an increasingly popular alternative to SPECT [10] and is now the recommended procedure for resin microspheres [1]. Post-treatment verification with PET exploits the fact that ^{90}Y can decay to the excited O$^+$ state of ^{90}Zr [11]. This state can then further decay through an internal pair production from an $E0$ transition with a branching ratio (BR) of $(3.26 \pm 0.04) \cdot 10^{-6}$ e^+e^- pairs per decay [12]. Despite this low BR, Ref. [10] showed more than a decade ago that a post-treatment verification with PET is feasible.

Recently, long axial field-of-view (LAFOV) PET/CT systems have found their way into clinical routine [13–18]. The sensitivity and noise equivalent count rate of LAFOV PET/CT systems significantly improves over standard field-of-view systems. For the imaging of ^{90}Y microspheres, LAFOV PET/CT outperform conventional PET/CT systems since it can compensate the low branching fraction of the excited ^{90}Zr state [19]. Furthermore, the limited FOV of conventional PET/CT

---

* Corresponding author.
E-mail address: lorenzo.mercolli@insel.ch (L. Mercolli).

Table 1

^{90}Y activities in at reference time and the dimensions of the background and sphere volumes of the NEMA IQ phantoms. The quoted errors are described in the text.

Volume name	Diameter [mm]	Volume [ml]	Activity [MBq]
cold bkg	N/A	9762.0 ± 98.5	0.0
hot bkg	N/A	9829.0 ± 97.8	1193.51 ± 0.18
s_1	10.0 ± 0.5	0.528 ± 0.079	0.64 ± 0.15
s_2	13.0 ± 0.5	1.16 ± 0.13	1.40 ± 0.27
s_3	17.0 ± 0.5	2.58 ± 0.23	3.12 ± 0.55
s_4	22.0 ± 1.0	5.61 ± 0.76	6.78 ± 1.40
s_5	28.0 ± 1.0	11.5 ± 1.2	13.9 ± 2.60
s_6	37.0 ± 1.0	26.6 ± 2.2	32.1 ± 5.60

systems and the resulting decrease in sensitivity towards edges of the FOV makes the imaging of the whole liver with a single bed position very challenging.

The aim of this study is to compare a dose calculation method that is based on LAFOV PET images with image independent methods. To this end, we performed phantom scans and computed the dose using two commercial software products: Hermes (Hermes Medical solutions, Stockholm, Sweden) and Simplicit90Y (Mirada Medical Ltd, Oxford, UK; Boston Scientific Corporation, Marlborough, MA, USA). Hermes' voxel dosimetry module uses a so-called semi-Monte Carlo (sMC) algorithm for the dose calculation and therefore requires quantitative PET images as input. Simplicit90Y computes the deposited dose assuming a local deposition model, which for the case of a phantom is independent of the PET image. Finally, we performed a Monte Carlo (MC) simulation with the software FLUKA [20–22], which provides the full modelling of the ^{90}Y decay, particle transport and dose deposition. It is completely independent of the imaging and segmentation process and therefore serves as the ground truth for the dose calculation.

2. Materials and methods

2.1. Measurements and imaging protocols

For the image acquisition of ^{90}Y with a LAFOV PET/CT, two NEMA International Electrotechnical Commission (IEC) body phantoms (Data Spectrum Corp.) [23,24] were filled with demineralized water, a minor addition of hydrochloric acid and ^{90}Y citrate. The total activity at reference time was 1.31 ± 0.20 GBq, while at scan time it had decayed to 1.12 ± 0.17 GBq. All activity measurements were carried out with an ISOMED 2010 well-type dose calibrator that was calibrated by the Swiss Federal Institute of Metrology METAS. The activity measurement of almost pure β emitters like ^{90}Y is challenging, in particular with well-type dose calibrators. In order to take into account the systematic error of the activity measurements (calibration factor, variations in the measurement geometry, filling levels, etc.), we assume an error of 15%, which is within the maximum admissible error for a calibrated system in Switzerland (see e.g. Ref. [25]).

One phantom had a hot and the second one a cold background. In Table 1 we report the activities inside the volumes of the six spheres and the background volumes of the phantoms. The sphere to background activity concentration ratio is approximately $1 : 10$ with an activity concentration of ≈ 1.3 MBq/ml in the spheres. The activities in the phantoms' spheres were lower compared to typical lesions that are treated with SIRT. The setup should therefore be considered as a rather challenging case for imaging and dose calculations.

The error on the sphere volumes are derived from the errors on the diameters quoted in the NEMA phantom specifications. These are the possible variations in the production process of the phantoms. The background volumes are determined through their weight when filled with demineralized water and we assume a 1% error on the weight measurement and a water density of 0.9982 g/ml according to the ICRU Report 90 [26].

The two phantoms were imaged with a Biograph Vision Quadra PET/CT scanner (Siemens Healthineers, Knoxville, TN, USA) at the Department of Nuclear Medicine, Inselspital, Bern University Hospital. The detectors of the Biograph Vision Quadra are made of 5×5 arrays of $3.2 \times 3.2 \times 20$ mm lutetium oxyorthosilicate (LSO) crystals that are coupled to a 16×16 mm array of silicon photomultipliers. 4×2 such mini-blocks are arranged into one detector block. The whole PET detector consists of 32 detector rings with 38 blocks each. This yields an axial FOV of 106 cm. All images were acquired with a maximum ring distance of 322 crystals (MRD 322) and reconstructed the images in ultra-high sensitivity mode (UHS). For comparison, images were also reconstructed in high sensitivity mode (HS) with a MRD of 85 crystals. The NEMA sensitivity for ^{18}F in UHS is 176 kcps/MBq, while in HS it is 83 kcps/MBq [16]. The time-of-flight (TOF) resolution of the Biograph Vision Quadra is 228 and 230 for HS and UHS, respectively. While the Biograph Vision Quadra's sensitivity exceeds the one of standard FOV scanners, the TOF and spatial resolution of $3.3 \times 3.4 \times 3.8$ mm are comparable to standard systems.

The images of the two phantoms were acquired during 50 min. Reconstructions were performed using a dedicated image reconstruction prototype (e7-tools, Siemens Healthineers). The error on the resulting dose does not include any error form the image reconstruction process. For the image reconstruction Siemens' TOF, point-spread function (PSF) recovery and ordered subset expectation maximization (OSEM) is used. According to Ref. [19], the optimal reconstruction parameters in terms of image quality for both HS and UHS are two iterations, five subsets, a 2 mm Gaussian filter and a 220×220 matrix. In order to assess the dependence dose calculation's dependence on the scan time, images were reconstructed with the first 5, 10 and 20 min of scan duration in UHS by rebinning the list-mode data. For comparison, we also reconstructed an image in HS mode with 20 min scan duration. Fig. 1 shows examples with UHS reconstruction and with 5 min and 20 min acquisition time. The decay correction and quantification for ^{90}Y is done directly by the vendor's image acquisition and reconstruction software. Of course, an uncertainty in the quantification of the activity concentration in the PET image could propagate to the image based dose calculation. Based on the recovery coefficients in Ref. [19] for the larger spheres and the reconstruction protocol described above, we assume a 10% error on the PET image quantification. Note that this is not included the 15% error from the activity measurement.

2.2. Dose calculations

The doses deposited in the phantom's spheres were calculated using three independent methods: a full MC simulation of the NEMA phantom, the image based sMC method from Hermes' voxel dosimetry module and Simplicit90Y's local deposition model.

The NEMA phantom was implemented in CERN's FLUKA 4-2.2 [20, 21] and Flair 3.1-15.1 [22], which is a general MC framework for particle transport. Fig. 2 shows the rendering of the phantom geometry and an example of the dose distribution. We used the standard PRECISIO setting of FLUKA for the physics and transport parameters (most importantly, the particle transport threshold is set to 100 keV). The simulations were run in semi-analogue mode, i.e. the ^{90}Y decay is simulated with random decay times, daughters and inclusive decay radiation, for every single sphere and the hot background separately. The simulation of the hot background required a dedicated source routine due to the non-standard shape of the background volume. The decay properties of ^{90}Y are taken in FLUKA's isotope library. The resulting doses were scored with the USRBIN routine in spherical regions (region binning) with the nominal size NEMA phantom spheres. This avoids volume errors from voxelization. Of course, the simulations's results need to be normalized to the measured total activities in Table 1. The simulation of 10^7 primaries were sufficient for reaching a negligible statistical error in the regional dose scoring and we do not assume any systematic error in the simulation itself (geometry implementation, ^{90}Y
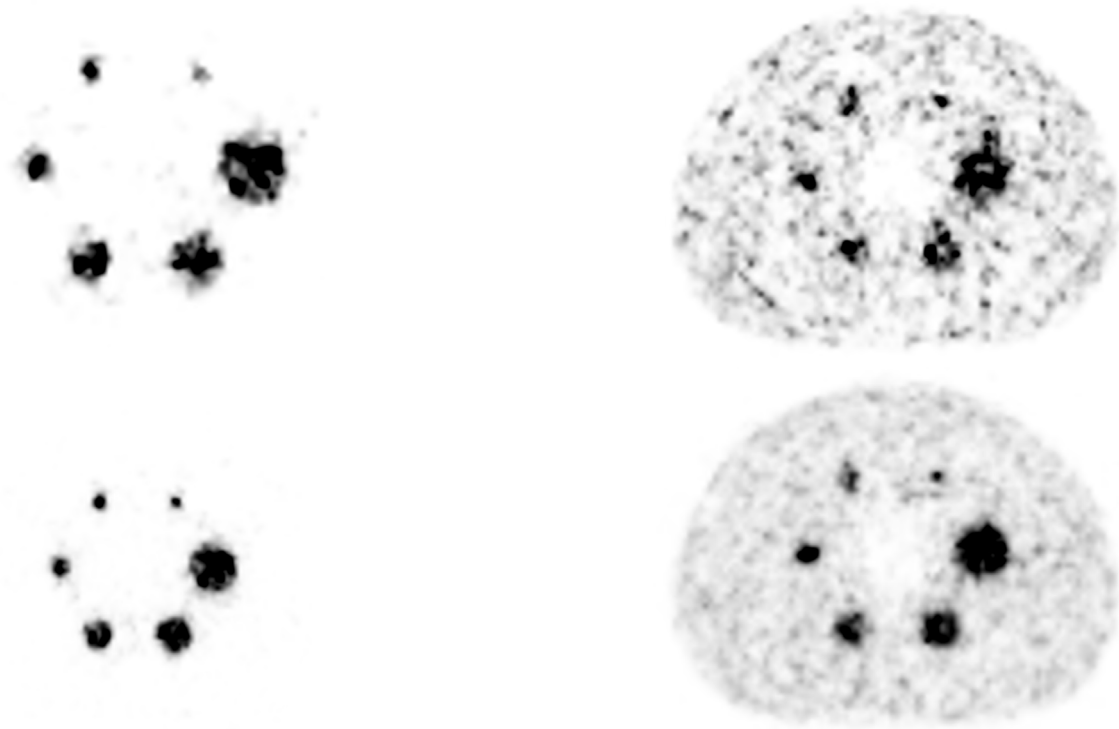
Fig. 1. Example images of UHS reconstruction and with 5 min (top) and 20 min (bottom) acquisition time for both cold and hot backgrounds.

Fig. 2. FLUKA implementation of the NEMA IQ phantom (left) and an illustrative example of a 3D dose distribution from FLUKA with cartesian grid scoring (right).

decay data, transport thresholds, etc.). Therefore, the uncertainties on the doses from the MC simulations stem only from the uncertainties related to the activity measurements shown in Table 1.

Hermes' voxel dosimetry module provides the possibility to calculate a dose map from a quantitative PET or SPECT image through the so called sMC method [27,28]. The authors of Ref. [28] proposed the sMC for the post-treatment dosimetry of lutetium-177 (^{177}Lu) peptide receptor radionuclide therapy in order to overcome the accurate but time consuming full MC calculations (see also Refs. [27,29]). The basic idea behind sMC is to separate the electron and photon transport: the electron's energy is absorbed locally, i.e. in the same voxel where the decay has been detected, while for the photons a point-wise transport is used. The algorithm first converts the activity distribution from and image to an electron dose map. Second, the photons are transported in a full MC down to a threshold of 15 keV [27]. The energy of photons with an energy below the transport threshold as well as the energy of recoil electrons is deposited locally. Note that for the photon transport sMC uses only cross sections of water, which are then rescaled to the various tissue densities [28].

With a mean electron energy of $\bar{E}_\beta = 148.8$ keV (79.44% intensity) and $Q_\beta = 496.8$ keV in conjunction with the low spatial resolution of SPECT images, ^{177}Lu is an ideal radionuclide for sMC. However, the

literature on sMC for other radionuclides, such as ^{90}Y or ^{131}I, is scarce and, as pointed out the authors of Ref. [27], further investigation for the applicability of sMC beyond ^{177}Lu is necessary.

The sMC implementation of Hermes allows for a truly image based voxel-wise dose calculation. Therefore, different scan times and reconstruction settings can lead to different doses. For every input image (in units of Bq/ml) Hermes computes a dose map, i.e. an image with units of Gy. For all dose maps, we used Hermes Hybrid Viewer to segment the phantom spheres. The volumes-of-interest (VOI) were drawn on the CT according to the nominal sphere diameters of the NEMA phantom. Since the dose scales with the inverse volume, segmenting the phantom spheres in the dose maps by a threshold (e.g. relative to some maximal voxel value) would make a comparison with the other dose calculation methods meaningless.

Hermes does not provide information on the statistical error of the voxel values of the dose map from the sMC method. As mentioned before, we do not consider any error from the image reconstruction but add a 10% uncertainty on the quantification. Hermes' Hybrid Viewer reports the volume of each (voxelized) VOI and the deviation from the nominal spheres can reach 10%.

In order to disentangle the systematic error from the sMC algorithm from the uncertainty of the activity distribution in the PET image, we

Table 2

Doses in Gy in the six spheres of the NEMA phantom with a cold background according to the different dose calculation methods.

Method	D_{s_1} [Gy]	D_{s_2} [Gy]	D_{s_3} [Gy]	D_{s_4} [Gy]	D_{s_5} [Gy]	D_{s_6} [Gy]
FLUKA	41.1 ± 8.9	46.0 ± 8.8	50.1 ± 8.8	53.2 ± 11.0	55.6 ± 10.0	57.7 ± 10.0
Simplicit90Y	46.8 ± 11.0	49.7 ± 11.0	45.6 ± 9.3	50.6 ± 12.0	52.8 ± 11.0	50.2 ± 10.0
UHS 50 min	26.2 ± 3.7	36.9 ± 5.2	34.7 ± 4.9	43.0 ± 6.1	44.6 ± 6.3	45.5 ± 6.4
UHS 20 min	20.8 ± 2.9	33.8 ± 4.8	32.0 ± 4.5	39.8 ± 5.6	42.3 ± 6.0	45.8 ± 6.5
UHS 10 min	18.6 ± 2.6	30.2 ± 4.3	29.8 ± 4.2	38.5 ± 5.4	39.6 ± 5.6	44.7 ± 6.3
UHS 5 min	9.07 ± 1.3	25.1 ± 3.5	29.6 ± 4.2	33.3 ± 4.7	35.0 ± 4.9	42.2 ± 6.0
HS 20 min	29.0 ± 4.1	39.3 ± 5.6	37.0 ± 5.2	41.0 ± 5.8	44.7 ± 6.3	48.9 ± 6.9

Table 3

Doses in Gy in the six spheres of the NEMA phantom with a hot background according to the different dose calculation methods.

Method	D_{s_1} [Gy]	D_{s_2} [Gy]	D_{s_3} [Gy]	D_{s_4} [Gy]	D_{s_5} [Gy]	D_{s_6} [Gy]
FLUKA	42.0 ± 9.0	46.8 ± 8.9	50.7 ± 8.8	53.7 ± 11.0	55.9 ± 10.0	58.0 ± 10.0
Simplicit90Y	46.8 ± 11.0	49.7 ± 11.0	45.6 ± 9.3	50.6 ± 12.0	52.8 ± 11.0	50.2 ± 10.0
UHS 50 min	24.5 ± 3.5	31.2 ± 4.4	36.1 ± 5.1	40.8 ± 5.8	45.6 ± 6.4	46.8 ± 6.6
UHS 20 min	24.8 ± 3.5	29.5 ± 4.2	32.5 ± 4.6	39.0 ± 5.5	41.8 ± 5.9	45.2 ± 6.4
UHS 10 min	30.4 ± 4.3	30.0 ± 4.2	36.1 ± 5.1	36.4 ± 5.1	40.5 ± 5.7	44.3 ± 6.3
UHS 5 min	31.7 ± 4.5	26.4 ± 3.7	31.4 ± 4.4	37.2 ± 5.3	37.6 ± 5.3	41.6 ± 5.9
HS 20 min	35.3 ± 5.0	35.4 ± 5.0	41.4 ± 5.9	41.9 ± 5.9	44.6 ± 6.3	48.2 ± 6.8

constructed a synthetic PET image and passed it through Herme's voxel dosimetry module. This synthetic PET image contains the spheres of the NEMA phantom with the nominal activities from Table 1 as well as the hot background. In the systematic error of the resulting doses, only the voxelization of the spheres stems from the synthetic PET image while the rest can be attributed to the sMC algorithm.

Lastly, the dose inside the phantom spheres was also computed with Simplicit90Y's multi-compartment dosimetry module (see e.g. Refs. [4, 7,30] for multi-compartment dosimetry). Simplicit90Y relies on a local deposition model with a homogeneous activity distribution [31]. The dose in a compartment or perfused volume is computed according to

$$\bar{D}_c = 50 \cdot \frac{A_c \cdot (1 - F) \cdot (1 - R)}{m} ,\tag{1}$$

where A_c is the activity in GBq inside the compartment and m is its mass in kg. In the phantom measurements the lung shunt fraction F and the residual waste fraction R were set to zero. According to the Simplicit90Y manual the dose factor is fixed at $50\,\text{Gy kg/GBq}$. Note that slightly lower values can be found in the literature (see e.g. Refs. [4,7]). In Simplicit90Y, all dose calculations assume a liver density of $1.06\,\text{g/cm}^3$. Since in the phantoms are filled with water, we corrected the doses from Simplicit90Y by the ratio of the liver and water density. Simplicit90Y only takes image information if there are overlapping volumes. This is not the case for the NEMA phantoms and therefore the dose calculation with Simplicit90Y is independent of the PET image. The constant dose factor is simply multiplied by the activities in Table 1. As in the case of the sMC dose calculation, the VOI were drawn as spheres with the size according to the nominal sphere diameters. There is some deviation from the exact spherical volume due to the voxelization of the volume (in the CT image) and possibly some rounding errors of Simplicit90Y. The uncertainties of the dose values from Simplicit90Y are therefore composed of a 10% error from the volume voxelization and the error on the activities inside the spheres in Table 1. We do not consider any systematic uncertainty on the local deposition model nor on the constant dose factor of $50\,\text{Gy kg/GBq}$.

3. Results

Tables 2 and 3 report the doses deposited in the six spheres of the cold and hot background phantoms. Fig. 3 visualizes the values in Tables 2 and 3. As previously mentioned, the FLUKA dose calculation is considered as the ground truth for the doses.

Fig. 3 shows an increase of dose from the MC simulation with increasing sphere diameter. In the case of the hot phantom this effect is slightly less pronounced. However, the error bars are large, due to the uncertainty of the activity measurement, and therefore this effect

is statistically insignificant. The Simplicit90Y doses vary depending on the sphere diameters and are exactly the same for both phantoms.

Compared to FLUKA and Simplicit90Y, the Hermes based dose calculations shows a systematic underestimation of the doses. This underestimation is particularly pronounced in the case of the two smallest spheres and for short acquisition times. In most cases the dose from the UHS images decreases with decreasing acquisition time. Interestingly, the HS based dose is comparable or even closer to the FLUKA dose than the dose from the and 50 min UHS image. While most of the Hermes dose values lie still within the 1σ range of the FLUKA doses, the systematic uncertainties of the Hermes calculation require some discussion.

In Fig. 4 we report the doses that stem from using a synthetic PET image with an optimal activity distribution as an input for Hermes' sMC algorithm. Compared to FLUKA, Hermes overestimates the doses for small sphere diameters.

4. Discussion

The increase of dose values from the MC simulation with increasing sphere diameter in Tables 2 and 3 is due to the width of the ^{90}Y dose point kernel (DPK), i.e. the smaller the sphere the higher the relative fraction of the dose is deposited outside the sphere. When comparing FLUKA's doses of the cold and hot background phantoms, we can see a similar effect in the sense that with increasing sphere diameter the relative amount of the spill-in dose from the hot background becomes smaller. Note however, that the uncertainty due to the activity measurement is rather large, making these effects statistically insignificant.

Since the ^{90}Y activity increases with the sphere volume but the dose decreases with the inverse volume, the doses from Simplicit90Y should in principle have the same value for all six spheres. However, due to the voxelization of the volumes in the CT images and the rounding errors of the volume in Simplicit90Y there is a variation in the doses for different sphere diameters in Fig. 3. Nevertheless, the doses computed with Simplicit90Y are comparable the FLUKA doses, in particular when taking into account the associated errors. Obviously, there is no difference between the cold and hot background doses since no information is taken from the PET images in Simplicit90Y in the absence of multiple compartments. In sum, the doses computed with Simplicit90Y confirm the fixed dose factor of $50\,\text{Gy kg/GBq}$ for larger volumes, hint towards issues with rounding errors for small volumes and show the inability to capture physical effects (width of ^{90}Y DPK) of the dose distribution in small volumes.

The doses values from Hermes in Fig. 3 offer an interesting comparison since they depend on the quantified PET images. Comparing
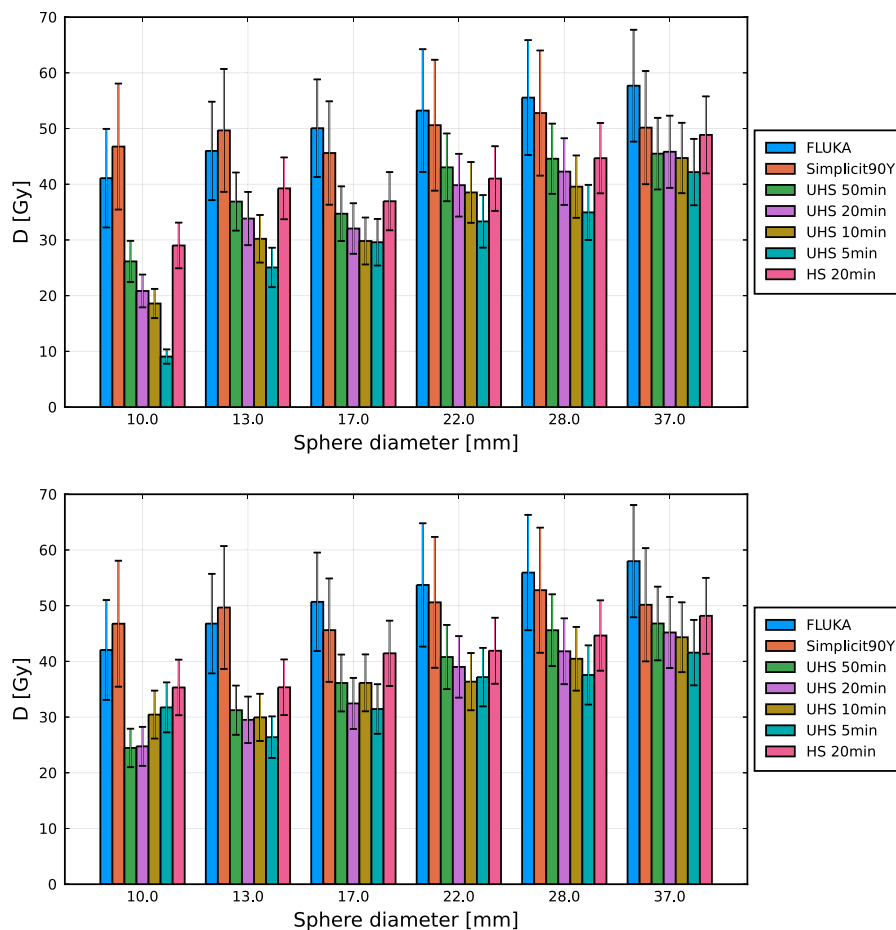
Fig. 3. Visualization of the doses in Tables 2 and 3 for the cold (top) and cold (bottom) background phantoms.
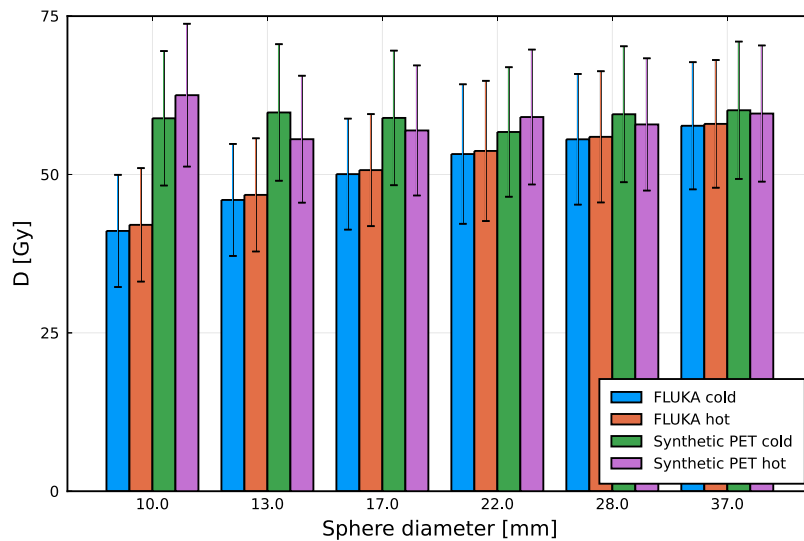

Fig. 4. Comparison between the doses from FLUKA and the Hermes doses from the synthetic PET image.

the different scan times in UHS mode, Fig. 3 seems to show that the Hermes doses become smaller for shorter scan times. This is particularly pronounced for the case of the smallest sphere and the cold phantom. It is tempting to conclude that longer scan times lead to dose values closer to the ground trough. However, our analysis shows that this trend is not statistically significant due to the relatively large error bars. Even if the image quality improves with scan time in general, as shown in

Ref. [19], the volume of the dose distribution remains small compared to the nominal sphere volume. Also Ref. [32] argues that longer scan times to not improve the results in such challenging imaging situations due to the LSO background radiation and the inherent blurring of ^{90}Y (imaged positrons stem from pair production of a high-energy prompt γ in the ^{90}Zr). Interestingly, the 20 min HS image seems to lead to doses that are comparable to the 50 min UHS image.

A priori, the systematic underestimation of the dose in the Hermes dose values compared to FLUKA can be either due to the quantification uncertainty in the PET image or due to the shortcomings of the sMC algorithm or both. Already the original authors pointed out that the assumptions underlying the sMC algorithm might not be applicable to ^{90}Y [28]. However, the result from the synthetic PET image in Fig. 4 shows that only for the smaller spheres, the sMC overestimates the deposited dose. Since the sMC algorithm deposits the β^- dose in the source voxel, there high β^- energy of ^{90}Y and the resulting dose spill-out, i.e. the width of the DPK, is not fully modelled. For the larger spheres, the dose spill-out becomes less relevant and the sMC results are consistent with FLUKA. This lets us conclude that Hermes' underestimation of the doses in Fig. 3 is dominated by the poor quantification of the activity distribution in the PET images. Indeed, the recovery coefficients in Ref. [19] do not reach 100%, even for the largest sphere.

Our results from the synthetic PET are in line with the results of Ref. [33]. For smaller spheres the activity distribution is not quantified well enough, even with a LAFOV PET system. While in Ref. [33] the a full MC dose calculation gives good results except for the smallest sphere, the sMC algorithm is limited to larger structures as shown in Fig. 4.

5. Conclusions

In this paper we compared different dose calculation methods for ^{90}Y radioembolization. While the full MC and Simplicit90Y dose calculations are independent of the input images, Hermes relies on the sMC algorithm to compute dose maps based on the activity distributions of images that were aquired with a LAFOV PET/CT.

The MC and Simplicit90Y dose calculations agree well within the error margins. Simplicit90Y's local deposition model is not able to catch the effect of the width of the ^{90}Y DPK, which is most visible in small volumes. Furthermore, the voxelization of the exact sphere volume in Simplicit90Y leads to a nonphysical variation of the dose values for different sphere diameters.

The Hermes' sMC method shows an underestimation of the dose for all input images compared to the full MC calculation. Processing a synthetic PET image revealed that while the sMC algorithm is unable to catch the width of the ^{90}Y DPK, the discrepancy in the dose based on the LAFOV images is driven by the poor quantification of the activity distribution in the PET images.

Our analysis implies several questions that should be addressed in the future. On one side, a benchmark Simplicit90Y's multi-compartment dose calculation based on LAFOV PET images would be very desirable. A thorough comparison of the accuracy of the post-treatment dosimetry with the pre-treatment dose prediction could indicate a true advantage of LAFOV systems for SIRT.

Declaration of competing interest

HS is a full-time employee of Siemens Healthcare AG, Switzerland. AR has received research support and speaker honoraria from Siemens. All other authors have no conflicts of interest to report.

References

[1] Levillain H, Bagni O, Deroose CM, Dieudonné A, Gnesin S, Grosser OS, et al. International recommendations for personalised selective internal radiation therapy of primary and metastatic liver diseases with yttrium-90 resin microspheres. Eur J Nucl Med Mol Imaging 2021;48(5):1570–84. http://dx.doi.org/10.1007/s00259-020-05163-5.

[2] Vilgrain V, Pereira H, Assenat E, Guiu B, Ilonca AD, Pageaux G-P, et al. Efficacy and safety of selective internal radiotherapy with yttrium-90 resin microspheres compared with sorafenib in locally advanced and inoperable hepatocellular carcinoma (sarah): An open-label randomised controlled phase 3 trial. Lancet Oncol 2017;18(12):1624–36. http://dx.doi.org/10.1016/S1470-2045(17)30683-6.

[3] Konijnenberg M, Herrmann K, Kobe C, Verburg F, Hindorf C, Hustinx R, et al. EANM position paper on article 56 of the council directive 2013/59/euratom (basic safety standards) for nuclear medicine therapy. Eur J Nucl Med Mol Imaging 2021;48:67–72. http://dx.doi.org/10.1007/s00259-020-05038-9.

[4] Dezarn WA, Cessna JT, DeWerd LA, Feng W, Gates VL, Halama J, et al. Recommendations of the american association of physicists in medicine on dosimetry, imaging, and quality assurance procedures for 90y microsphere brachytherapy in the treatment of hepatic malignancies. Med Phys 2011;38:4824–45. http://dx.doi.org/10.1118/1.3608909.

[5] Giammarile F, Bodei L, Chiesa C, Flux G, Forrer F, Kraeber-Bodere F, et al. EANM procedure guideline for the treatment of liver cancer and liver metastases with intra-arterial radioactive compounds. Eur J Nucl Med Mol Imaging 2011;38:1393–406. http://dx.doi.org/10.1007/s00259-011-1812-2.

[6] Tafti BA, Padia SA. Dosimetry of y-90 microspheres utilizing tc-99 m spect and y-90 pet. Semin Nucl Med 2019;49(3):211–7. http://dx.doi.org/10.1053/j.semnuclmed.2019.01.005, radioembolization of Liver Malignancies.

[7] Dieudonné A, Hobbs RF, Sanchez-Garcia M, Lebtahi R. Absorbed-dose calculation for treatment of liver neoplasms with 90y-microspheres. Clin Transl Imaging 2016;4(4):273–82. http://dx.doi.org/10.1007/s40336-016-0195-6, cited by: 4.

[8] Brosch J, Gosewisch A, Kaiser L, Seidensticker M, Ricke J, Zellmer J, et al. 3D image-based dosimetry for yttrium-90 radioembolization of hepatocellular carcinoma: Impact of imaging method on absorbed dose estimates. Phys Med 2020;80:317–26. http://dx.doi.org/10.1016/j.ejmp.2020.11.016.

[9] Elschot M, Vermolen BJ, Lam MGEH, de Keizer B, van den Bosch MAAJ, de Jong HWAM. Quantitative comparison of pet and bremsstrahlung spect for imaging the in vivo yttrium-90 microsphere distribution after liver radioembolization. PLoS One 2013;8:e55742. http://dx.doi.org/10.1371/journal.pone.0055742.

[10] Lhommel R, Goffette P, Van den Eynde M, Jamar F, Pauwels S, Bilbao JI, et al. Yttrium-90 TOF PET scan demonstrates high-resolution biodistribution after liver SIRT. Eur J Nucl Med Mol Imaging 2009;36(10):1696. http://dx.doi.org/10.1007/s00259-009-1210-1.

[11] Basu SK, Mccutchan EA. Nuclear data sheets for A=90. Nucl Data Sheets 2020;165:1–329. http://dx.doi.org/10.1016/j.nds.2020.04.001.

[12] Dryák P, Šolc J. Measurement of the branching ratio related to the internal pair production of y-90. Appl Radiat Isot 2020;156:108942. http://dx.doi.org/10.1016/j.apradiso.2019.108942.

[13] Cherry SR, Jones T, Karp JS, Qi J, Moses WW, Badawi RD. Total-body pet: Maximizing sensitivity to create new opportunities for clinical research and patient care. J Nucl Med 2018;59(1):3–12. http://dx.doi.org/10.2967/jnumed.116.184028.

[14] Badawi RD, Shi H, Hu P, Chen S, Xu T, Price PM, et al. First Human Imaging Studies with the EXPLORER Total-Body PET Scanner. J Nucl Med 2019;60(3):299–303. http://dx.doi.org/10.2967/jnumed.119.226498.

[15] Spencer BA, Berg E, Schmall JP, Omidvari N, Leung EK, Abdelhafez YG, et al. Performance evaluation of the uEXPLORER total-body PET/CT scanner based on NEMA NU 2-2018 with additional tests to characterize PET scanners with a long axial field of view. J Nucl Med 2021;62(6):861–70. http://dx.doi.org/10.2967/jnumed.120.250597.

[16] Prenosil GA, Sari H, Fürstner M, Afshar-Oromieh A, Shi K, Rominger A, et al. Performance characteristics of the biograph vision quadra PET/CT system with a long axial field of view using the NEMA NU 2-2018 standard. J Nucl Med 2022;63:476–84. http://dx.doi.org/10.2967/jnumed.121.261972.

[17] Dai B, Daube-Witherspoon ME, McDonald S, Werner ME, Parma MJ, Geagan MJ, et al. Performance evaluation of the pennpet explorer with expanded axial coverage. Phys Med Biol 2023;68(9):095007. http://dx.doi.org/10.1088/1361-6560/acc722.

[18] Alberts I, Hünermund J-N, Prenosil G, Mingels C, Bohn KP, Viscione M, et al. Clinical performance of long axial field of view PET/CT: A head-to-head intra-individual comparison of the Biograph Vision Quadra with the Biograph Vision PET/CT. Eur J Nucl Med Mol Imaging 2021;48:2395–404. http://dx.doi.org/10.1007/s00259-021-05282-7.

[19] Zeimpekis KG, Mercolli L, Conti M, Sari H, Prenosil G, Shi K, et al. Phantom-based evaluation of yttrium-90 datasets using biograph vision quadra. Eur J Nucl Med Mol Imaging 2023;50(4):1168–82. http://dx.doi.org/10.1007/s00259-022-06074-3.

[20] Ahdida C, Bozzato D, Calzolari D, Cerutti F, Charitonidis N, Cimmino A, Coronetti A, et al. New capabilities of the FLUKA multi-purpose code. Front Phys 2022;9:705. http://dx.doi.org/10.3389/fphy.2021.788253.

[21] Battistoni G, Boehlen T, Cerutti F, Chin PW, Esposito LS, Fassò A, et al. Overview of the FLUKA code. Ann Nucl Energy 2015;82:10–8, joint International Conference on Supercomputing in Nuclear Applications and Monte Carlo 2013, SNA MC 2013. Pluri- and Trans-disciplinarity, Towards New Modeling and Numerical Simulation Paradigms. http://dx.doi.org/10.1016/j.anucene.2014.11.007.

[22] Vlachoudis V. Flair: A powerful but user friendly graphical interface for FLUKA. In: International conference on mathematics. Computational methods & reactor physics 2009, 2009, p. 790–800.

[23] Greer K. NEMA IEC body phantom set user's manual. Data Spectrum Cooperation; 2002.

[24] NEMA standards publication NU 2-2018: Performance measurements of positron emission tomographs. 2018.

[25] Bochud F, Spring P, Baechler S, Twerenbold D, Linder R, Leibundgut F. Dose calibrators quality controls in Switzerland: Six years of experience. 2006.

[26] ICRU report 90, key data for ionizing-radiation dosimetry: Measurement standards and applications. 2016.

[27] Hippeläinen E, Tenhunen M, Sohlberg A. Fast voxel-level dosimetry for 177Lu labelled peptide treatments. Phys Med Biol 2015;60:6685–700. http://dx.doi.org/10.1088/0031-9155/60/17/6685.

[28] Hippeläinen ET, Tenhunen MJ, Mäenpää HO, Heikkonen JJ, Sohlberg AO. Dosimetry software Hermes Internal Radiation Dosimetry: from quantitative image reconstruction to voxel-level absorbed dose distribution. Nucl Med Commun 2017;38:357–65. http://dx.doi.org/10.1097/MNM.0000000000000662.

[29] Hippeläinen E, Tenhunen M, Mäenpää H, Sohlberg A. Quantitative accuracy of 177Lu SPECT reconstruction using different compensation methods: Phantom and patient studies. EJNMMI Res 2016;6:16. http://dx.doi.org/10.1186/s13550-016-0172-0.

[30] Lotter K, Diemling M, Sohlberg A, Wiedner H, Haug A, Maringer FJ. Comparing calculated and experimental activity and dose values obtained from image-based quantification of 90Y SPECT/CT Data. Zeitschrift für Medizinische Physik 2021;31(4):378–87. http://dx.doi.org/10.1016/j.zemedi.2021.03.005.

[31] Mirada Medical Inc. Simplicit90Y 2.4.0 help guide. R2 Ed. 2021.

[32] Hesse M, d'Abadie P, Lhommel R, Jamar F, Walrand S. Yttrium-90 tof-pet-based eud predicts response post liver radioembolizations using recommended manufacturer fdg reconstruction parameters. Front Oncol 2021;11. http://dx.doi.org/10.3389/fonc.2021.592529.

[33] Costa G, Spencer B, Omidvari N, Foster C, Rusnak M, Hunt H, et al. Radioembolization dosimetry with total-body 90y pet. J Nucl Med 2022;63(7):1101–7. http://dx.doi.org/10.2967/jnumed.121.263145.